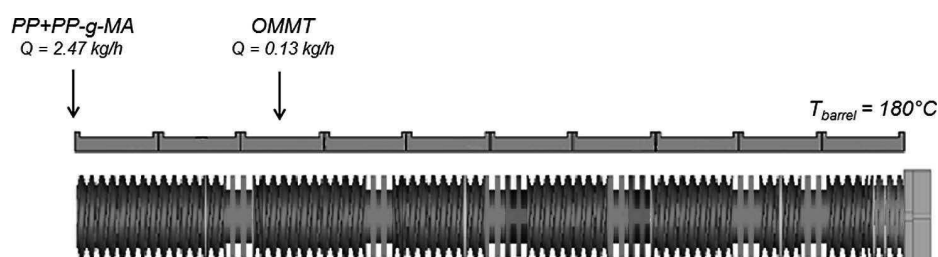


## ■ 1.4 Application to Twin-Screw Extrusion

### 1.4.1 Influence of the Processing Conditions on the Final Microstructure

To test the influence of the processing conditions on the OMMT dispersion, a laboratory-scale extruder was chosen, the screw profile of which is shown in Figure 1.7. The screws have a diameter of 24 mm and a length of 960 mm ( $L/D = 40$ ). The barrel is made up of 10 elements. The pre-blend of PP and PP-g-MA pellets is introduced into barrel 1, while the OMMT is fed into barrel 3, after the melting zone. Except for the first, all the barrel elements are set at 180 °C. After the melting zone, the screw profile consists of screw conveying elements, and five blocks of kneading discs, with various staggering angles. The formulation is kept constant and equal to 85 : 10 : 5 (PP-PP-g-MA-OMMT, in wt%).



**Figure 1.7** Screw profile used in the experiments

#### 1.4.1.1 Influence of the Screw Speed

In a first step, the screw speed was varied between 100 and 1100 rpm, at a constant total feed rate of 2.6 kg/h. The results are presented in Figure 1.8. The dispersion of the OMMT agglomerates improved when the screw speed increased, at least up to 600 rpm. Above this value, the dispersion was less efficient and larger agglomerates were present. Similarly, the yield stress (and thus exfoliation) increased up to around 400 rpm, and then stabilized at a lower level. Indeed, at high screw speed, a considerable overheating was observed: the final temperature increased from 192 to 238 °C between 100 and 1100 rpm. At 600 rpm, the temperature was high enough (222 °C) to induce thermal degradation of the organic modifier [22]. This was confirmed by a decrease in the interlamellar distance, from 3.8 to 3.6 nm, shown by XRD. Furthermore, the rheological characterizations showed that, above 300 rpm, a significant mechanical degradation of the matrix developed, resulting in a decrease in the weight average molecular weight, from 123 kg/mol for the virgin PP to 103 kg/mol at 1100 rpm [24]. Therefore, if an increase in screw speed helps to improve OMMT dispersion [25–29], it appears that excessively high speeds are not recommended for the preparation of nanocomposites.

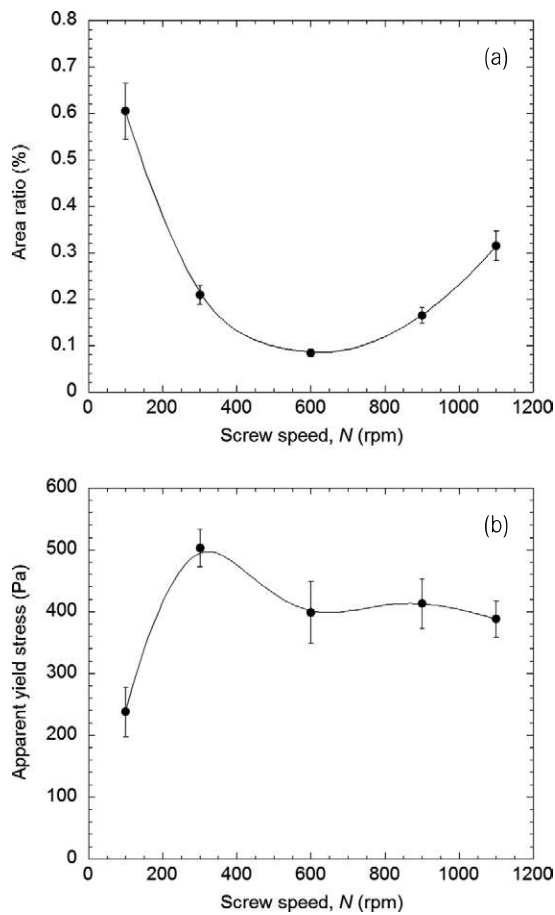


**Figure 1.8**  
Changes in area ratio (a) and apparent yield stress (b) with the screw speed (2.6 kg/h, 180 °C) (reprinted from [24])

#### 1.4.1.2 Influence of the Feed Rate

The experiments were carried out on the same lab-scale extruder, but with a slightly different screw profile. For these experiments, a masterbatch dilution method was chosen: in the first step, a 40 : 40 : 20 masterbatch (PP-PP-g-MA-OMMT, in wt%) was prepared. It was then diluted with PP in a second step, to obtain a final 85 : 10 : 5 nanocomposite. In this case, the pre-blend of masterbatch and PP pellets was introduced into the main hopper, that is, into barrel 1. The barrel temperature was set at 180 °C and the screw speed at 500 rpm in order to allow a wide range of variation of the feed rate. This high value of the screw speed was possible here because the selected screw profile was less severe than in the previous section. It is clearly shown in Figure 1.9 that an increase in feed rate induced an increase in area ratio and a decrease in apparent yield stress [30, 31]. In other words, the quality of the dispersion, both at the micro- and the nanoscale, decreased with the feed rate. In fact, an increase in the feed rate essentially affects the residence time, with a sharp decrease of the mean residence time and a narrowing of the distribution [10]. This link between residence time and exfoliation was also cited by Dennis et al. [32].

Consequently, the effect of the feed rate in the twin-screw extrusion is similar to that of the mixing time in the internal mixer (see Figure 1.5).

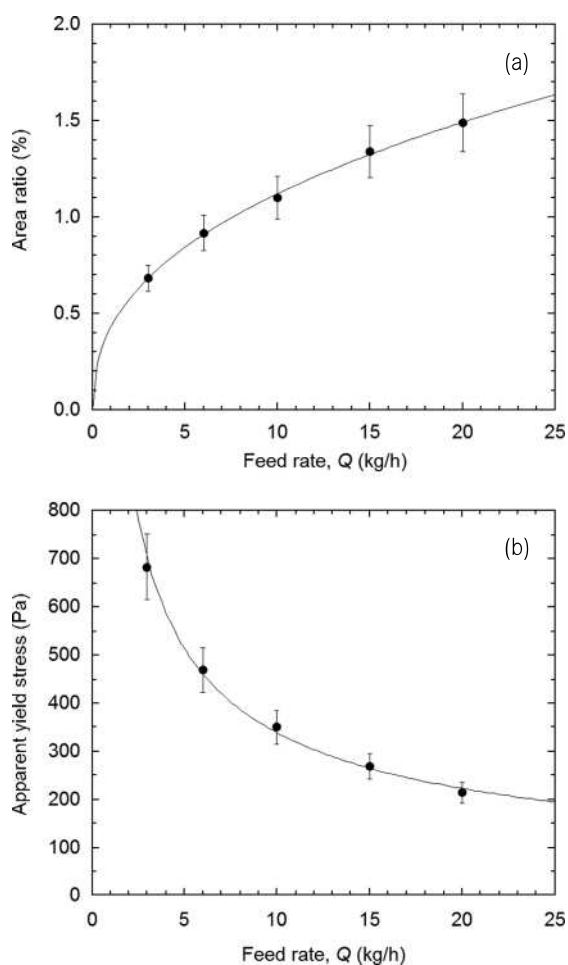


**Figure 1.9**

Changes in area ratio (a) and apparent yield stress (b) with the feed rate (500 rpm, 180 °C) (reprinted from [30])

The XRD measurements showed an intercalated structure, with an increase in the interlayer distance with feed rate, except at the lowest feed rate (3 kg/h) where this distance was less than that of the pristine OMMT [6]. Since the final temperature was about 210 °C, irrespective of the feed rate, we can imagine that the long residence time at 3 kg/h (about 2 min) was responsible for a thermal degradation of the organic modifier.

#### 1.4.1.3 Influence of the Barrel Temperature

Masterbatch dilution was also carried out, at 300 rpm and 3 kg/h, for a barrel temperature varying between 180 and 240 °C. The results are presented in Fig-

ure 1.10. The effect is similar to that of the feed rate, but less significant: an increase in barrel temperature increased the area ratio and decreased the yield stress. At high temperatures, the aggregates were larger, probably because the viscosity and thus the shear stresses were lower.

The XRD measurements indicated an intercalated structure (interlayer distance between 3.4 and 3.5 nm), except at 240 °C where it was lower (3.3 nm) than the pristine OMMT. In this last condition, the final temperature of the nanocomposite was about 260 °C, resulting in the destruction of the intercalant. The decrease of the apparent yield stress is, as for the area ratio, explained by the decrease of the stresses. To summarize, a high barrel temperature is detrimental to the quality of the dispersion of the OMMT, as already reported in the literature [5, 27, 33].

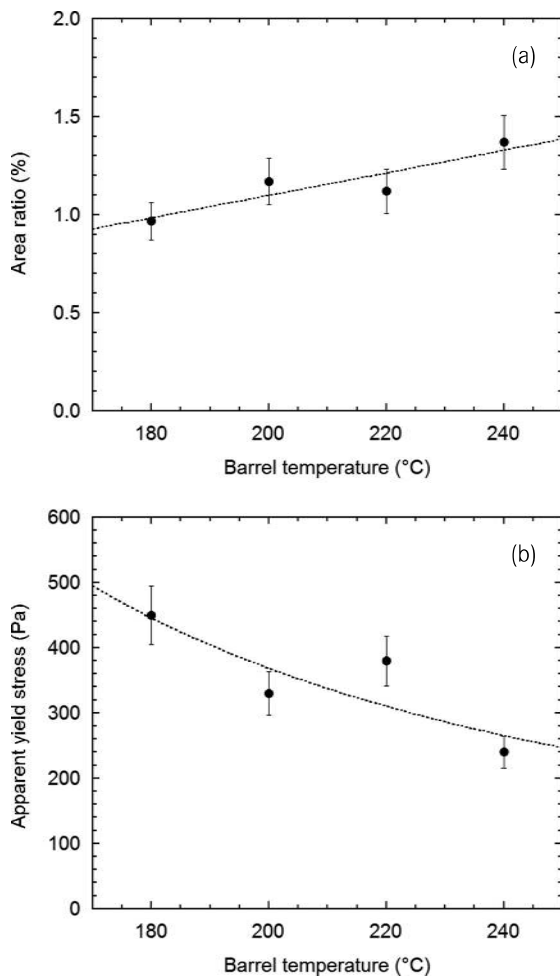


**Figure 1.10**

Changes in area ratio (a) and apparent yield stress (b) with the barrel temperature (300 rpm, 3 kg/h) (adapted from [6])

#### 1.4.1.4 Conclusions

As for the internal mixer, the results presenting the influences of the processing parameters (screw speed, feed rate, and barrel temperature) can be summarized when they are plotted versus the SME measured on the extruder (Figure 1.11). While the area ratio decreases steadily, the yield stress increases linearly up to 600 kWh/t and then stabilizes at a value of about 700 Pa.

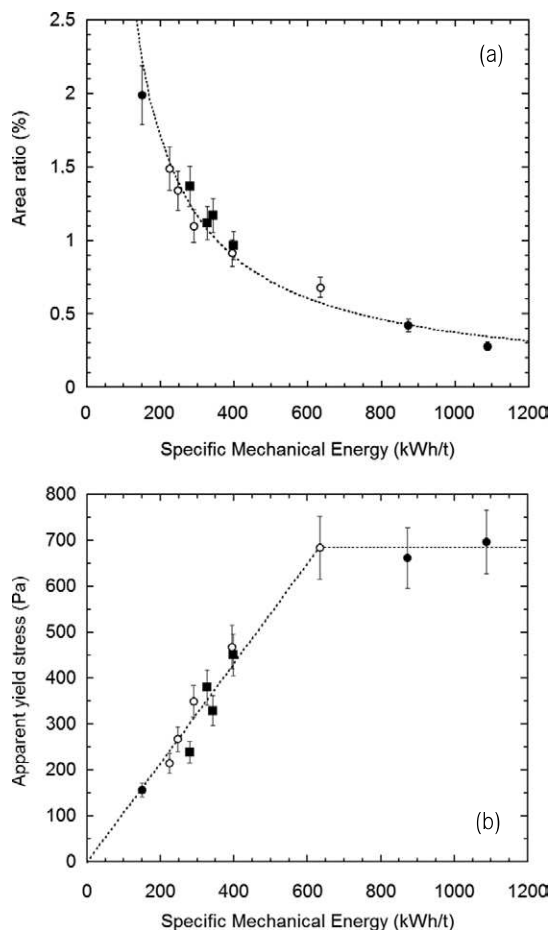


**Figure 1.11**

Changes in area ratio (a) and apparent yield stress (b) with the specific mechanical energy (SME). (●): effect of screw speed, (○): effect of feed rate, (■): effect of barrel temperature (reprinted from [30])

Even if they were obtained on two different systems (direct OMMT dispersion and masterbatch dilution), the results of the internal mixer and the twin-screw extruder are interesting to compare. In Figure 1.12(a), we observe that the agglomerate dispersion is much worse on the twin-screw extruder. This is explained by the preparation of the masterbatch, where the high quantity of the OMMT (20 wt%) has led to the formation of large and solid agglomerates that are difficult to disperse thereafter. On the other hand, changes in yield stress with SME are in good agree-

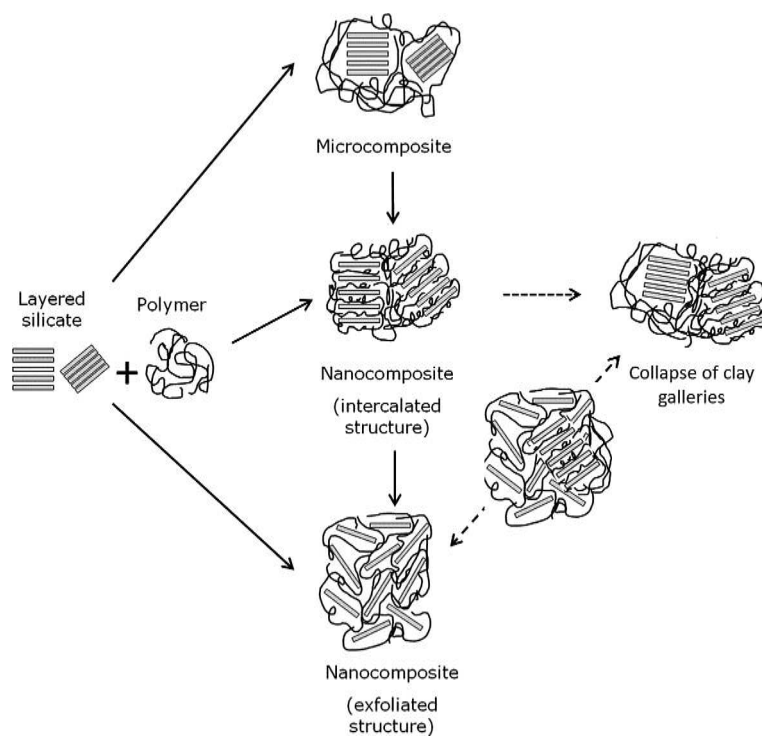


**Figure 3.3** Dispersion mechanism of layered organoclays into polymer matrices taking into account the possible collapse of the clay galleries due to the thermal degradation of the clay surfactant and polymer

### ■ 3.3 Carbon Nanotubes

Carbon nanotubes (CNTs) are formed by a hexagonal lattice of  $sp^2$  hybridized carbon atoms wrapped into a cylindrical shape. CNTs can be formed as single-walled (SWCNTs) or multi-walled (MWCNTs), the former consisting of an individual graphene layer rolled up into a cylindrical shell with a diameter of 1–2 nm, whereas the latter contains several cylindrical shells coaxially arranged and stacked, separated by a distance of 0.34 nm. CNTs have outstanding mechanical and thermal properties, with typical values for a Young's modulus of 1 TPa, tensile strength  $>50$  GPa, thermal conductivity  $>3000 \text{ W m}^{-1} \text{ K}^{-1}$ , and electrical conductivity in the range  $10^6$ – $10^7 \text{ S m}^{-1}$ . This set of excellent properties makes them attractive for applications in conductive polymer composites and adhesives, energy storage, thermal conductors, structural composite materials, microelectronics, etc. [33, 34]. However, in practice, it has been demonstrated that attaining full performance is not easy, not only because commercial CNTs contain impurities (e.g., metal cata-

lyst particles and amorphous carbon), they also lack dimensional uniformity, form stable agglomerates, and are difficult to disperse in polymer matrices. This created a trough of disillusionment in the 2000s, and their commercial sustainability was questioned. In recent years, a better understanding of the chemical-physical characteristics and dispersion mechanisms, together with advances in manufacturing technologies and in surface functionalization, has promoted a new upsurge in the practical interest in CNTs.

The dispersion of carbon nanoparticles in polymeric matrices is difficult because:

- in the pristine state,  $\pi$ – $\pi$  stacking and van der Waals interactions between individual tubes may lead to significant attraction and formation of stable agglomerates;
- MWCNTs grow as highly entangled agglomerates of several microns or even millimeters;
- the surface chemical inertia of CNTs due to the lack of chemical functionalities prevents the creation of strong interfaces with polymer molecules.

Interestingly, it is now generally accepted that perfectly dispersed CNTs are required for maximum mechanical reinforcement; however, the existence of a few agglomerates is not always detrimental and may be necessary to build up an effective conductive network. Consequently, the survival of initial agglomerates or the development of secondary agglomerates during mixing with a polymer may be advantageous for electrical conductivity. Therefore, understanding the dispersion mechanisms of CNTs is of major importance for the practical production of nanocomposites with a tailored CNT dispersion extent to achieve optimal performance.

Dispersion of CNTs may be facilitated by surface modification of the particles and/or compatibilization with the polymer matrix (albeit this strategy may affect the transport properties). Chemical modification can be accomplished by non-covalent and covalent approaches [35, 36]. Through electrostatic, van der Waals, or  $\pi$ – $\pi$  stacking interactions, the former enables the attachment and stabilization of different functional groups at the surface of the CNTs without disturbing their carbon structure and electronic network. However, this method is unsuitable for melt mixing – which is the focus of this chapter – as the functionalization compounds are usually unstable at the typical polymer processing temperatures. Covalent functionalization involves bonding chemical groups to the carbon atoms of the CNTs' surface, changing their hybridization state and decreasing their conjugation through the formation of covalent bonds. This method may induce surface damage and affect the electrical conductivity; however, if the covalent functionalization approach is conveniently selected, the resulting functionalized CNTs are appropriate for melt mixing.

### 3.3.1 Dispersion of Carbon Nanotubes

The dispersion of CNTs in thermoplastic polymers during melt mixing has been the focus of numerous studies, using various types of mixing equipment and processing conditions. These studies converged to a number of general observations that enabled the build-up of phenomenological dispersion models such as that illustrated in Figure 3.4. Dispersion of the CNT agglomerates requires their wetting and infiltration by the polymer melt, reducing the agglomerate cohesion strength. The ease of infiltration of the polymer melt depends mainly on the agglomerate density and size [37], on the polymer interfacial tension [38], and viscosity. Pötschke and co-workers [39–42] found a correlation between dispersibility of CNTs and bulk density of the initial CNT agglomerates. Similarly, Salzano de Luna et al. [43] observed that CNT particles consisting of small and loosely packed clusters formed by interwoven bundles of combed yarns of nanotubes were easier to disperse than the reference denser commercial counterparts. Interfacial tension is not relevant when the hydrophobic CNTs are to be dispersed in polar polymers (e.g., polyamide, polycarbonate, polyimide). In the case of non-polar polymers (e.g., polyolefins), it is necessary to incorporate surface functionalities to the CNTs as mentioned above.

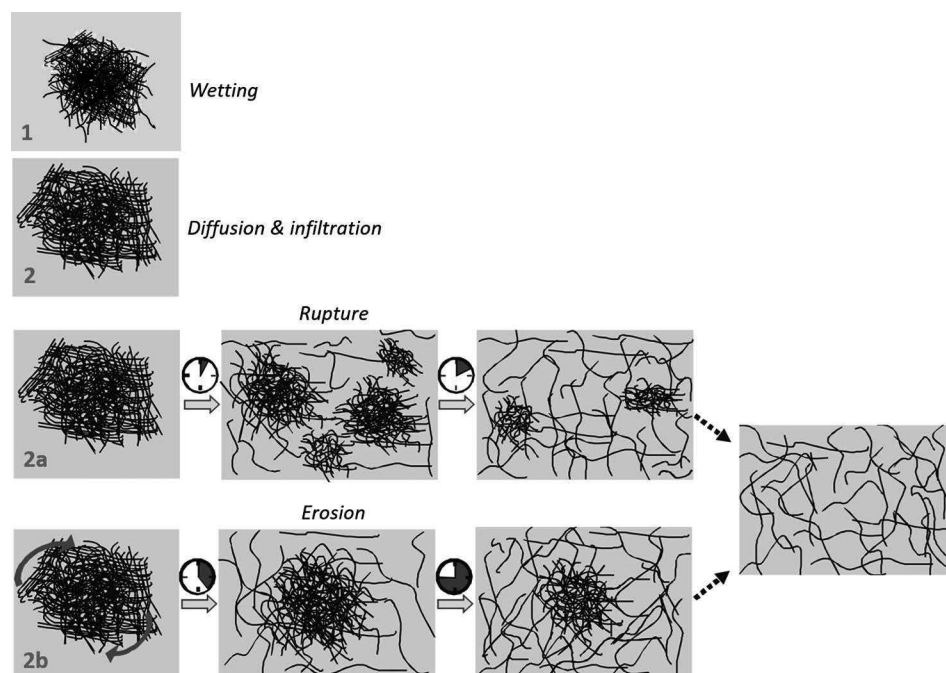


**Figure 3.4** Dispersion mechanisms of CNT agglomerates in a polymer melt (adapted from [45, 48])



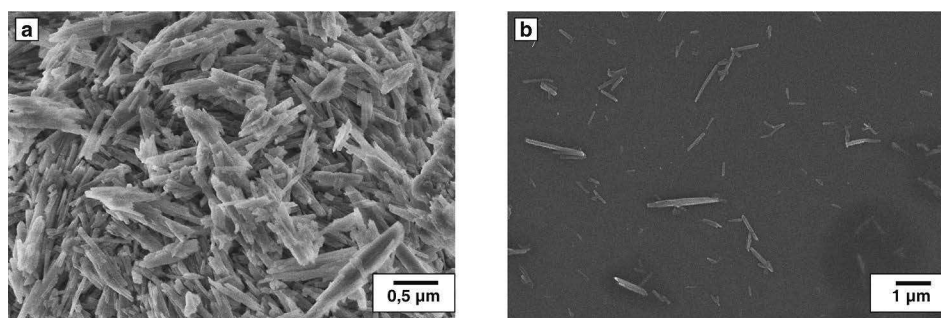
After creating the ideal sharp crack tip, the threshold value of the fatigue crack propagation  $\Delta K_{th}$  is determined. For this purpose,  $\Delta K$  is reduced with a constant  $\Delta K_{gradient}$  of  $-0.03 \text{ MPa}\cdot\text{m}^{1/2}/\text{mm}$  until the  $da/dN$  value reaches  $10^{-7} \text{ mm/cycle}$ . Below  $\Delta K_{th}$ , no crack propagation occurs. In order to restart crack propagation,  $\Delta K$  is increased rapidly by a given  $\Delta(\Delta K)$  of  $0.03 \text{ MPa}\cdot\text{m}^{1/2}$ . Finally, the fatigue crack propagation behavior is determined as a function of  $\Delta K$ . In order to achieve it,  $\Delta K$  is increased with a constant  $\Delta K_{gradient}$  of  $0.03 \text{ MPa}\cdot\text{m}^{1/2}/\text{mm}$  and the fatigue crack propagation rate  $da/dN$  is thus determined. These measurements were performed using a maximum  $a/w'$  ratio of 0.8.

## ■ 4.4 Results and Discussion

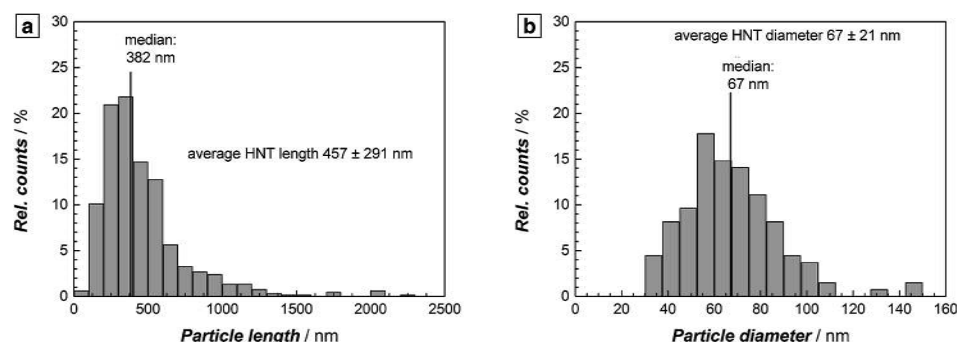
### 4.4.1 Multiscale Material Characterization

#### 4.4.1.1 Particle Morphology and Particle Size Distribution

The HNTs used herein are characterized by a homogenous nanotube morphology and are almost free of non-tubular impurities (Figure 4.5a). However, the as-received HNTs are strongly agglomerated and have to be dispersed prior to chemical modification. Figure 4.5b depicts an SEM image of HNTs after an ultrasonic treatment in aqueous solution. The agglomerates were broken and isolated HNTs were observed. In order to quantify the particle sizes, SEM pictures of dried droplets of a highly diluted HNT suspension were evaluated regarding the lengths and diameters of the HNTs (Figure 4.6). The particle lengths of the more than 400 characterized HNTs range from 70 nm to 2200 nm with a median of 382 nm. The average length is  $457 \text{ nm} \pm 291 \text{ nm}$ . The diameter of the nanotubes ranges from 30 nm to 146 nm. The median is 67 nm and the average diameter is  $67 \text{ nm} \pm 21 \text{ nm}$ . Consequently, the average aspect ratio of the nanoparticles is approximately 7. The HNTs' length distribution as well as the mean HNTs' length remained unaffected by the HNTs' dispersion carried out in the three-roll mill.



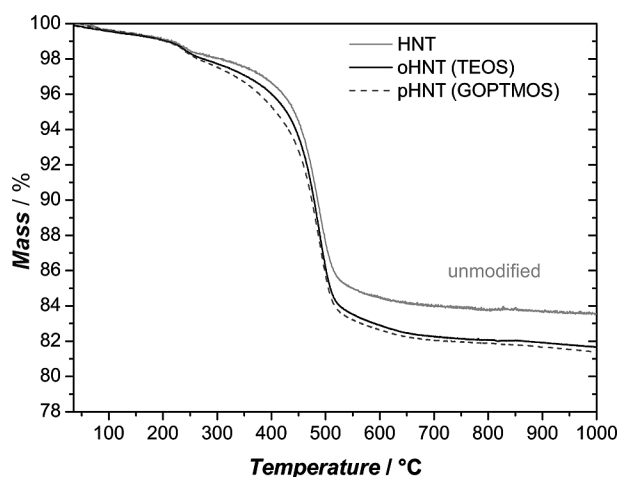
**Figure 4.5** SEM images of HNTs (a) as-received and (b) isolated particles after the ultrasonication process in water (200 W)



**Figure 4.6** Particle length (a) and diameter distribution (b) of the HNTs after the ultrasonic treatment

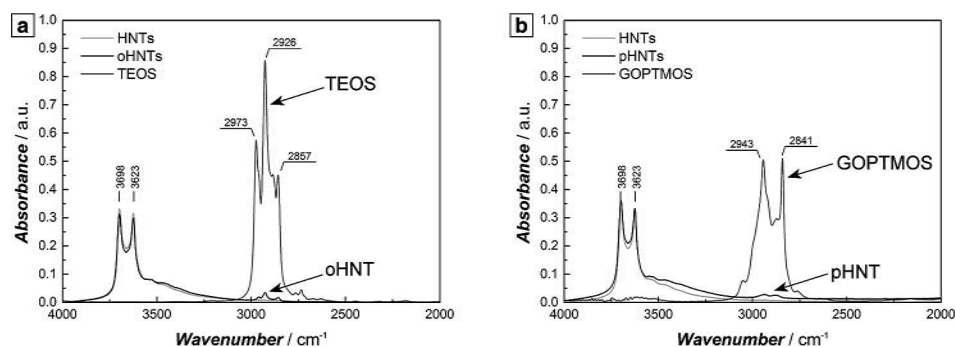
#### 4.4.1.2 Characterization of the HNTs' Modification

The results of the TGA analysis of unmodified, and TEOS (oHNTs)- and GOPTMOS (pHNTs)-modified HNTs are shown in Figure 4.7. The total mass loss of unmodified HNTs is 16.5 wt%. The first regime of the unmodified particles from 100 to 250 °C exposes a slight mass loss due to organic impurities absorbed on the HNTs' surface. The decomposition of the surface hydroxyl groups is detected in the range from 250 to 550 °C. The modified HNTs show a similar behavior, whereas an additional weight loss is observed at above 250 °C attributed to the decomposition of the grafted silanes to the HNTs' surface. A grafting weight of 1.9 wt% is calculated for oHNTs and 2.1 wt% for pHNTs.

**Figure 4.7**

TGA measurements of unmodified and modified HNTs

Furthermore, FTIR measurements confirm the presence of the silanes on the HNTs' surface (Figure 4.8). Compared to the spectrum of unmodified HNTs, the TEOS-modified HNTs (oHNTs) (Figure 4.8a) clearly show additional peaks at around 2800 to 3000  $\text{cm}^{-1}$ , which are characteristic of C–H vibrations and also present in the spectrum of the pristine silane. Similar results are obtained for GOPTMOS-modified HNTs (pHNTs) (Figure 4.8b); however, in the pHNT spectrum, the peaks associated with the C–H bands hardly appear.

**Figure 4.8** FTIR analysis of (a) oHNTs and (b) pHNTs in comparison to as-received HNTs

The silane grafting is also evidenced by XPS measurements as shown in Table 4.2. The carbon content of 4.3 wt% of the unmodified HNTs is due to organic impurities, which are also detected by TGA measurements. The oHNTs and pHNTs show an increased carbon content of 18.1 wt% and 10.8 wt%, respectively, indicating successful surface modification. XPS measurements show a decrease in the atomic contents of the silicon, aluminum, and oxygen components of the HNTs' surface

[7]. By comparing the two types of modified HNTs, the increase in carbon content and decrease in oxygen content are less pronounced for pHNT as compared to oHNT. Since GOPTMOS consists of a lower number of carbon atoms and a higher number of oxygen atoms, these differences are thus reasonable.

**Table 4.2** Surface Composition of HNTs in wt%, Determined by XPS Analyses

Atom	HNT (as-received)	oHNT (TEOS)	pHNT (GOPTMOS)
C	4.3	18.1	10.8
Si	17.8	15.5	17.2
Al	15.1	12.7	13.6
O	62.7	53.7	58.4

The assumed chemical structure of the pHNT surface modification is depicted in Figure 4.9. Since the modification is carried out in an aqueous solution, the epoxy functionality is hydrolyzed during the grafting reaction [39].

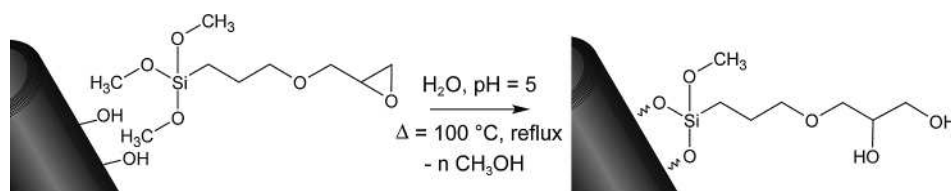


**Figure 4.9** Hydrolysis of the epoxy functionality during the silane grafting reaction in aqueous media, according to Horr et al. [39]

Finally, the real filler content of the nanocomposites was determined by TGA measurements, considering the determined weight loss of the HNTs of 16.5 wt% as seen in Table 4.3.

**Table 4.3** Real HNTs' Weight Fractions and Glass Transition Temperature of the Nanocomposites

Intended content (wt%)	Unmodified HNTs		oHNTs (TEOS)		pHNTs (GOPTMOS)	
	Content (wt%)	$T_g$ (°C)	Content (wt%)	$T_g$ (°C)	Content (wt%)	$T_g$ (°C)
0	-	150 ± 1	-	150 ± 1	-	150 ± 1
1.25	1.2 ± 0.1	147 ± 1	1.4 ± 0.1	150 ± 1	1.3 ± 0.1	147 ± 1
2.5	2.4 ± 0.1	149 ± 1	2.9 ± 0.3	150 ± 1	2.3 ± 0.1	146 ± 1
5.0	4.8 ± 0.1	146 ± 1	4.8 ± 0.1	151 ± 1	4.4 ± 0.2	138 ± 1

#### 4.4.1.3 Dispersion of the HNTs

The morphologies of the nanocomposites are examined by scanning and transmission electron microscopy techniques. SEM images of the fracture surfaces of the nanocomposites with the highest HNT contents (4.8 wt% HNTs, 4.8 wt% oHNTs, and 4.4 wt% pHNTs) provide a good overview of existing agglomerates (Figure 4.10a–c). The morphology of the nanocomposites filled with unmodified HNTs (image (a)) is characterized by a lot of agglomerates in the range of 5–10  $\mu\text{m}$ . However, the surface treatment of the HNTs leads to less agglomeration as revealed by images (b) and (c). For both modifications, TEOS and GOPTMOS, the number and the size of clusters are significantly reduced. TEM images (Figure 4.10d–f) support these observations by revealing big agglomerates in the case of unmodified HNTs and mainly individually separated HNTs for oHNTs and pHNTs. Regardless of the type of surface treatment, the HNTs' dispersion is improved although the presence of some small agglomerates could not be avoided.

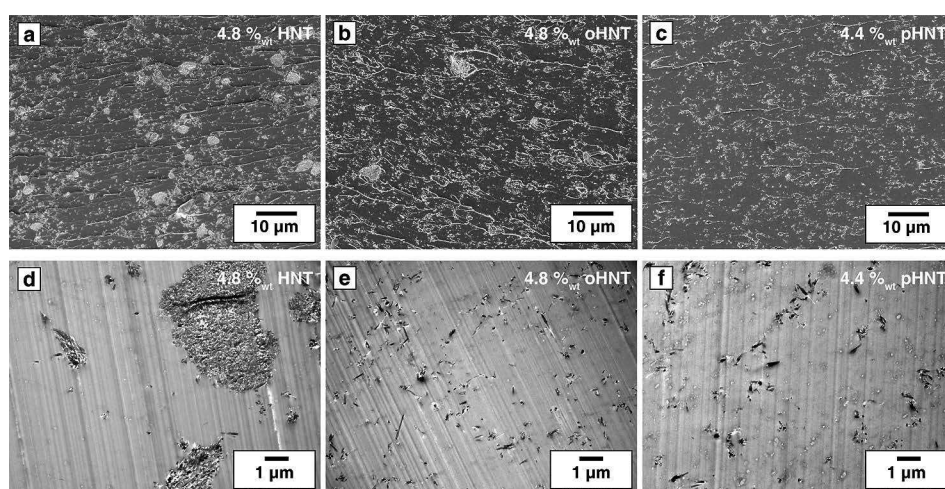


**Figure 4.10** SEM (a–c) and TEM (d–f) micrographs of the nanocomposites containing 4.8 wt% unmodified HNTs (a and d), 4.8 wt% oHNTs (b and e), and 4.4 wt% pHNTs (c and f)

#### 4.4.1.4 Influence of Surface Modification on Interface Chemistry

It is important to mention that the interface chemistry is highly influenced by the composition and molecular structure of the resin system. The anhydride cured epoxy network is characterized by a large number of polar groups, most importantly, the hydrophilic carbonyl groups corresponding to the methylhexahydrophthalic anhydride monomers. On the contrary, the bisphenol A backbone of the DGEBA monomers is highly hydrophobic. As a consequence, the interactions between the HNTs and the matrix are strongly affected by their compatibility, determined by the type of surface modifier.

decreased with increasing number of layers in the sheet. When Rahman et al. [58] studied the viscosity contrast effect on the foam morphology and layer integrity, they found that using a high viscosity resin for the film layer and a low viscosity resin for the foam layer produced better layer integrity. The film layer with the high viscosity acted as a confining layer, which helped reduce the cell size of the foamed layer as the nominal layer thickness decreased. Guo et al. [55, 56] investigated the extension rheology of different polyolefins and their blends to improve their foaming ability using multilayer coextrusion. These studies mostly focused on neat polymer foams without conductive filler networks.

In the work reported here, a multilayer coextrusion process was used to fabricate a polystyrene/CNT (PS/CNT) sheet to study the effect of multilayer coextrusion on the morphology evolution and conductivity of coextruded PS/CNT composites when the layer thickness varies from the macroscale to the sub-microscale. The effect of matrix viscosity on the morphology and resistivity was also studied. It was found that viscosity plays a role in the behavior and that low viscosity materials were more sensitive to layer multiplying, particularly at sub-micron layer thicknesses. Additionally, the multilayer and foaming approaches were combined as an approach for improving EMI shielding. The multilayer coextrusion processes was used to extrude a sheet with alternating layers of a CNT-filled polymer foam and neat solid polymer. The main objective of this work was to investigate the effect of the number of layers, CNT content, and foaming agent content on the morphology of these materials. The EMI shielding properties were measured and correlated to the material morphology.

## ■ 7.2 Experimental

### 7.2.1 Materials

The CNTs were obtained as a commercially available 20 wt% polystyrene (PS)/CNT masterbatch (MB2020-00, Hyperion Catalysis). The CNTs were vapor-grown multi-wall carbon nanotubes with a reported diameter, length, and density of 10–15 nm, 1–10  $\mu\text{m}$ , and 1750  $\text{kg}/\text{m}^3$ , respectively.

The CNT masterbatch was diluted with two commercially available polystyrenes: Ineos Nova 3601 (MI = 13.5 g/10 min, density = 1040  $\text{kg}/\text{m}^3$ , estimated molecular weight = 168,000 Da [59]) and Americas Styrenics LLC's Styron 665 (MI = 1.5 g/10 min, density = 1040  $\text{kg}/\text{m}^3$ , molecular weight = 305,000 Da [60]). Since the molecular weight (MW) of Styron 665 was 1.8 times greater than the molecular weight of Nova 3601, these polystyrenes were designated as high MW PS and low MW PS, respectively.

The polystyrene (PS) compounds for the foamed layer were prepared by diluting the PS/CNT masterbatch with a commercially available polystyrene (Americas Styrenics LLC, grade: Styron 685D). This polystyrene was also used for the neat film layer. A commercial endothermic chemical foaming agent (Bergen International, grade: Foamazol™ 95) was used to foam the PS/CNT layer. For this foaming agent, the suggested processing temperature for a maximum gas yield was 175 to 200 °C.

CNT-filled PS was fabricated by diluting the 20 wt% PS/CNT masterbatch to 3 and 5 wt% PS/CNT compounds using a co-rotating twin screw extruder (Leistritz, ZSE18HP-400). For the foamed trials, the PS-CNT masterbatch was diluted into compounds with 1.5, 3.0, and 6.0 wt% CNTs. The masterbatch and neat PS pellets were fed separately into the twin screw extruder by two volumetric feeders to provide the correct CNT loadings. All compounds were prepared using a temperature profile of 150 to 200 °C (rear to die), a constant screw speed of 300 rpm, and an output of about 3.6 kg/h. The extrudate was cooled and pelletized for coextrusion.

### 7.2.2 Coextrusion of Multilayer Samples

The coextrusion line had two 25-mm Wayne single screw extruders ( $L/D = 30:1$ ), two Zenith PEP gear pumps, a customized feedblock, and layer multiplying elements (LMEs). The customized feedblock was designed to form a three-layer “sandwich” profile (shown in Figure 7.1). Melt from the feedblock was fed into the LMEs, where the melt streams were split (1), stacked (2), and merged (3). The number of individual layers in the extrudate,  $N$ , was directly proportional to the number of LMEs,  $n$ , added to the coextrusion line:

$$N = 2^{(n+1)} + 1 \quad (7.1)$$

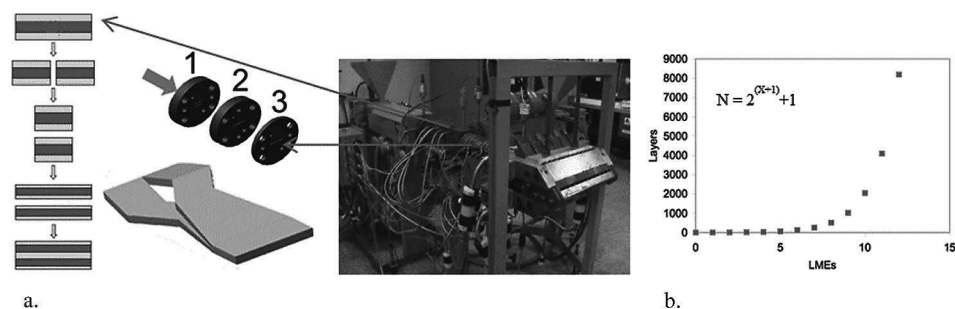


**Figure 7.1** (a) Layer multiplying coextrusion set-up and schematic plot of a horizontal layer multiplication process and (b) the relationship between number of layers and number of layer multiplying elements

For the PS/CNT systems, the twin screw compounded material was fed into both extruders of the coextrusion line and the two melt streams were pumped into the feedblock using gear pumps for tight control of the output. The PS/CNT sheet with nominal individual layers ranging from 3 to 8193 was fabricated using 0 to 12 LMEs. Table 7.1 lists the processing temperatures of LMEs and feedblock, number of LMEs, and CNT concentration for each coextrusion trial. The output was held constant at about 2.4 kg/h and the feed ratio for the two extruders was 50:50. In order to analyze the effects of LMEs on the compounds, no sheet die was used in the process. All samples were directly extruded from the LMEs onto the roll stack. To achieve the optimal surface finish and efficient cooling, extruded melts were mounted and cooled on the chilling rolls with a rotation speed of 0.6 m/min.

**Table 7.1** Processing Trials at Different Temperatures Utilizing 0 to 12 LMEs

Number of LMEs	Number of Layers	$T_{\text{LME}} = 210\text{ }^{\circ}\text{C}$		$T_{\text{LME}} = 230\text{ }^{\circ}\text{C}$	
		CNT Concentration (wt%)		CNT Concentration (wt%)	
		High MW PS	Low MW PS	High MW PS	Low MW PS
0	3	3	3	5	5
3	17	–	3	–	–
7	257	–	3	5	5
12	8193	3	3	5	5

For the foamed samples, the pellets of diluted PS/CNT material were first dry blended with the foaming agent and then extruded as the middle layer of the sandwich structure that formed in the feedblock. The top and bottom layers (layers with a light color) of the sandwich structure were neat PS melt, which was extruded from another extruder. After passing through the feedblock, the three-layer melt stream was pumped through three different sets of LMEs (0, 2, and 3), which corresponded to 3, 9, and 17 layers of melt. The feed ratio for the two extruders was 50:50 and the output was held constant at about  $2.31 \times 10^{-3} \text{ m}^3/\text{h}$ . For the extruders, feedblock, and LMEs, the temperature was held constant at  $190\text{ }^{\circ}\text{C}$ ; a lower temperature of  $160\text{ }^{\circ}\text{C}$  was used for the sheet die to create the high pressure drop needed for the foaming process. To achieve the optimal surface finish and a constant sample thickness (1.5 mm), extruded foam/film multilayer sheets were pulled at a rate of 0.6 m/min on the chill rolls. The cooling temperature was  $60\text{ }^{\circ}\text{C}$ . Specific CNT and foaming agent usage for each trial are listed in Table 7.2. Since CNTs were only present in the foamed layer, the CNT content was calculated with respect to the total polymer material based on the 50:50 feed ratio in the coextrusion process.



**Table 7.2** Processing Trials for the Foamed Multilayer Sheet

Number of Layers	Nominal Individual Layer Thickness	[CNT] <sup>*</sup>		[Foaming Agent] <sup>**</sup>
	( $\mu\text{m}$ )	(wt%)	(vol%)	(wt%)
3	750	0	0	1, 2, and 3
		0.75	0.45	2
		1.51	0.90	2
		3.03	1.83	1, 2, and 3
9	187.5	3.03	1.83	2
17	93.75	0.75	0.45	2
		1.51	0.90	2
		3.03	1.83	1, 2, and 3

<sup>\*</sup> CNT content was calculated based on the total volume of the polymer in the extrudate.

<sup>\*\*</sup> Foaming agent concentration was based on the weight of the foam layer.

### 7.2.3 Characterization

Thermal gravimetric analysis (TGA) was carried out (TA Instruments Q50). To determine the CNT content in the compounded material, approximately 20 mg of diluted PS/CNT compound was placed in the platinum testing pan and heated from room temperature to 300 °C at a heating rate of 20 °C/min. The CNT content was calculated based on the weight loss after burning off the polymer in a N<sub>2</sub> atmosphere; neat PS was used as the baseline. The decomposition kinetics of the foaming agent was also performed using TGA [61]. A foaming agent pellet was first heated at a rate of 50 °C/min from about 20 °C to the processing temperature (190 °C) and then the isothermal test was conducted at 190 °C to measure the weight loss of foaming agent vs. time. The gas release during the process was estimated based on the weight reduction for the residence time of the coextrusion (6 minutes).

A capillary rheometer (Dynisco, LCR 7000) was used to characterize the flow behavior of both the 3 wt% and 5 wt% PS/CNT compounds prepared by twin screw extrusion. In accordance with ASTM D3835, the apparent viscosity of the compounds was measured at shear rates of 5, 10, 20, 40, 100, and 200 s<sup>-1</sup> and the two processing temperatures (210 and 230 °C). The data obtained from these measurements were corrected by the Weissenberg–Rabinowitsch correction to plot the corrected viscosity as a function of corrected shear rate.

Transmission electron microscopy (TEM) was used to characterize the dispersion, distribution, and orientation of the CNTs in the extrudate with different numbers of layers. The PS/CNT pellets were cut into ultrathin sections using a cryo-ultramicrotome (Leica, model: EM UC6) with a sharp glass knife and dropped on the

increasing probability of CNTs to come into contact with each other [9, 10]. Thus, it was a matter of a trade-off between the aggregation rate and the disaggregation rate. Disentangled MWCNTs were easily oriented in the flow direction while the MWCNTs within the agglomerations did not undergo alignment. Thus, shear rate broke the agglomerations and released more dispersed CNTs that aligned. Hence, higher shear rates were linked to higher orientation. These results agree with what is presented in Equation (10.1). A study on orientation as a result of shear and elongational deformation found that part of an intertwined CNT bundle could be “oriented” as a whole with each individual CNT within the agglomerate randomly oriented after elongational flow, while the others separated into individual CNTs. Pegel et al [8] and Handge et al [9] showed that the alignment state of CNTs in polycarbonate following elongational flow tends to experience relaxation. The results show that after 60 minutes, the orientation of the particles was random. Lele et al. [12] used X-ray diffraction to evaluate the flow-induced orientation of layered silicates in polypropylene compatibilized with maleic anhydride polypropylene. They demonstrated that clay tactoids were readily oriented in shear. He et al. [13] incorporated CNTs into natural rubber latex and followed their orientation during shear by Raman and TEM (transmission electron microscopy). They found that shear induced the CNTs’ alignment. Dykes et al. [14] showed by X-ray scattering measurements that nanoclays dispersed in polymers align relative to the flow direction and this depends on shear rate and applied strain amplitude, with almost no relaxation after flow cessation.

Recently, the principles of flow-induced orientation of elongated and rigid moieties were applied to nanoparticles by Kenig [15] in view of experimental results from the literature [7–13] that indicated that NCs or CNTs are oriented due to shear or elongation flows.

## ■ 10.3 Orientation Modelling

Jeffery [16] was the first to describe the orientation development of dilute elongated particles in a Newtonian fluid. Jeffery’s equation for simple shear is as follows:

$$\Phi_1' = \frac{\dot{\gamma}}{2} (1 + B \cos \Phi_1) \quad (10.1)$$

where  $\Phi_1'$  is the rate of angle change,  $\Phi_1$  is the orientation angle, and  $\dot{\gamma}$  the shear rate.

Integration of Equation (10.1) with time,  $t$ , results in Equation (10.2):

$$\tan \Phi_1 = (1 + B) / (1 - B^2)^{1/2} \tan \left\{ (1 - B^2)^{1/2} \times 2 \dot{\gamma} t \right\} \quad (10.2)$$

where  $B = (Rp^2 - 1) / (Rp^2 + 1)$ ,  $Rp$  is the aspect ratio of the elongated particle, and  $t$  the time of flow.

As Equation (10.2) suggests, the orientation angle (tangent) is related to the aspect ratio  $Rp$  and the product of shear rate and time – the total shear.

In the case of elongational flow, Jeffery's equation for diluted concentrations and Newtonian fluid could be written as:

$$\Phi_1' = B / 2 (\varepsilon' \sin \Phi_1) \quad (10.3)$$

where  $\varepsilon'$  is the elongation rate.

Integration of Equation (10.3) with respect to time leads to Equation (10.4):

$$\tan \Phi = C DR^{-\lambda} \quad (10.4)$$

where  $DR$  is the draw ratio equal to the product  $\varepsilon' \times t$  and the ratio  $D_1^2/D_2^2$ , where  $D_1$  is the initial extrudate diameter and  $D_2$  is the final drawn polymer diameter.  $\lambda$  is the "orientability parameter" depending on the  $Rp$  and adopted from Erickson's definition of anisotropic fluids [17].

As concluded from Equation (10.4), the orientation of an elongated particle in a simple elongational flow is related to the total elongation and the tendency of the particle to elongate in a specific fluid (the orientability parameter).

Finally, it was assumed that in high orientations (small  $\tan \Phi$ ), the modulus of elasticity is inversely proportional to  $\tan \Phi$ . Hence,

$$\tan \Phi = K/E \quad (10.5)$$

where  $K$  is the proportion constant.

Advanced models for the prediction of elongated particles (short fibers) orientation were suggested by Tucker and Folgar [18], especially to treat concentrated fiber compounds, taking into account fiber-fiber interactions. As nanocomposite melts are diluted in nature, the particles' interaction is minimized and the main concern is the nanoparticle-polymer interactions, which will be investigated in the present work.

The modified Jeffery's Equation (10.2), (10.4), and (10.5) will be the basis for the study on the orientation development of nanoparticles in elongation and shear flows.

## ■ 10.4 Methodology

Assuming that the two basic flow mechanisms – elongation and shear – control the orientation development during the processing of thermoplastics, the following methodology was followed:

The elongation mechanism was investigated using a simple unidirectional melt drawing system. In this part of the study, the effect of draw-down ratio (total elongation strain) on the modulus of CNTs and INTs containing polycarbonate (to avoid crystallinity induced by the nanoparticles) was investigated.

The shear mechanism was studied in using a parallel plate rheometer where the total shear depends on the number of revolutions and rotation speed.

In both flows, the total elongation and shear strains were calculated and the resulting orientation was determined using the elastic modulus (Equation (10.5)).

## ■ 10.5 Experimental

### 10.5.1 Materials Processes and Mechanical Characterization

Multiwalled carbon nanotubes (MWCNTs) (Nanocyl 7000 Belgium) with an elastic modulus of close to 1000 GPa, a strength of 10–65 GPa, a diameter of 10 nm, and a length of up to mms were used.

Multiwalled inorganic nanotubes ( $\text{WS}_2$  INTs) (NanoMaterials Israel) with an elastic modulus of 170 GPa, a strength of up to 16 GPa, a diameter of 80 nm, and a length of 1–20  $\mu\text{m}$  were used.

Polycarbonate (Makrolon 2207) was compounded with a 15% CNTs masterbatch (Nanocyl PC1501) to obtain 1 wt% and 0.5 wt% CNTs/PC nanocomposites.

Polycarbonate was compounded with inorganic nanotubes (INTs). The compounds were prepared with a twin screw extruder (Prism).

The storage modulus was determined by a dynamic mechanical analyzer (DMA) at room temperature.

### 10.5.2 Shear Orientation by Parallel Plate Rheometer

Circular specimens were prepared by compression molding of compounded PC/NTs.

A parallel plate rheometer was used to apply pure shear stresses using controlled one-direction rotation and varying rotation speeds as shown in Figure 10.1.

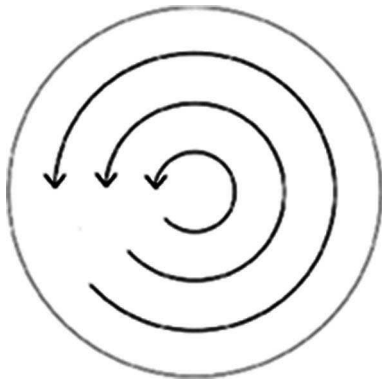


**Figure 10.1**  
Schematics of flow in a parallel plate rheometer

The shear rate of the parallel plate rheometer is given by

$$\dot{\gamma}(r) = \frac{r\Omega}{h} \quad (10.6)$$

where  $\dot{\gamma}(r)$  is the shear rate as a function of radius  $r$ ,  $r$  is the radial distance from the center of the circular plate,  $\Omega$  is the rotation speed, and  $h$  the thickness of the sheared material (Figure 10.2).

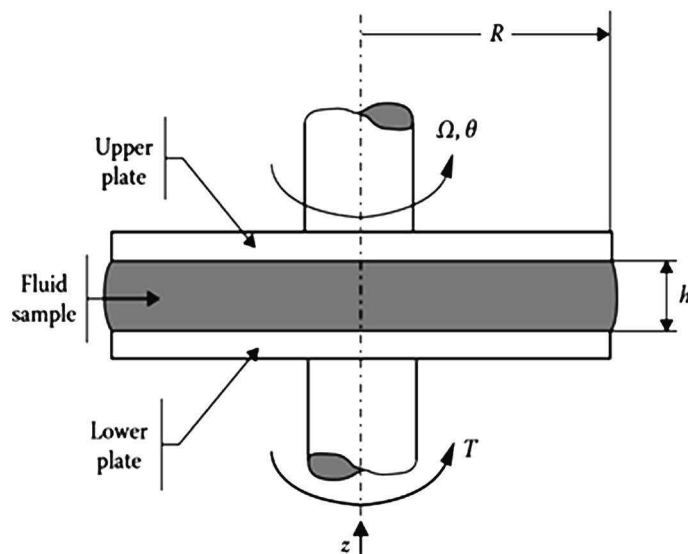


**Figure 10.2** Schematics of the parallel plate rheometer

To study the effects of shear on orientation, different total shears were applied on the molten nanocomposite melts. Following shear, the specimens were cooled to room temperature. DMA (dynamic mechanical analysis) tensile specimens were prepared from the circular specimens, as shown in Figure 10.3. The diameter of the circular disc was 25 mm. The specimens cut for the DMA measurements were 3 mm wide and 2 mm thick.

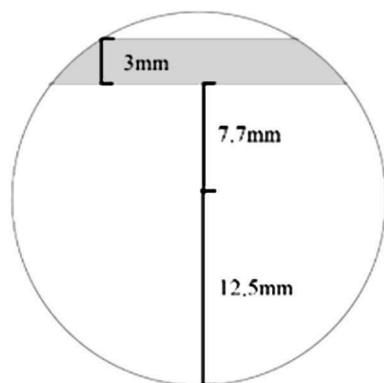


**Figure 10.3**

Location of specimens cut from the circular disc for DMA measurements

The shear rates, shear time, and total shear applied are given in Table 10.1.

**Table 10.1** Different Shear Rates, Times, and Total Shear Applied on the Nanocomposite Melts

Run	Angular velocity [rad/s]	Shear time [s]	Total shear
1	0.027174	240	30
2	0.054348	240	60
3	0.081522	240	90
4	0.108696	240	120
5	0.13587	240	150
6	0.217391	90	90

### 10.5.3 Elongational Orientation by Melt Drawing

The elongational flow was obtained by winding a polymer melt extrudate at different winding speeds, as shown in Figure 10.4.

### 13.3.6 Solvent Casting

In addition to those long, tedious, and costly preparation methods [31–36, 45], simple and efficient preparation methods, such as solvent casting, have been developed [19, 20]. This is similar to that introduced for hydro-soluble polymers (Figure 13.2) with the exception of the use of a non-aqueous medium. It has been reported that CNCs are dispersible in *N,N*-dimethylformamide (DMF) [19–21], dimethyl sulfoxide (DMSO) [33], formic acid [46], dimethylacetamide (DMAc) [47], pyridine [48], and a few more solvents. Therefore, the use of one of these solvents is a practical way for preparing polymer–CNC nanocomposites comprising a soluble polymer in the mentioned solvent, such as PLA [19, 20] and polyamide [46]. This method can also be used to produce masterbatches to be mixed with commercial grade polymers via conventional melt-mixing processes to prepare final polymer–CNC nanocomposites [18, 21, 48]. Likewise, masterbatches of hydro-soluble polymer–CNCs can be obtained by solvent casting as mentioned earlier and then melt- or solution-mixing with non-hydro-soluble polymers to prepare the final nanocomposites [16, 35]. The non-hydro-soluble polymer, often used as a compatibilizer, could bring complexities to the final nanocomposites' properties and it may not be desirable in terms of renewability, biocompatibility, and biodegradability [35]; or in some cases, it may countervail the reinforcing effect of the CNCs on the mechanical performances of the final nanocomposites [16, 47]. In addition, the miscibility of the compatibilizer with the polymer matrix is another concern.

## ■ 13.4 Effect of CNCs on the Properties of Polymers

### 13.4.1 Effect of CNCs on the Rheological Behavior of the Polymers

During the last few decades, rheology has been employed as a powerful tool to understand the interactions between the components of polymer nanocomposites. The formation of an interconnected network of particles plays an important role on the rheological behavior of nanocomposites that can reveal the efficiency of the preparation method leading to a micro or nano dispersion. Therefore, the effects of CNCs on the rheological behavior of molten polymer nanocomposites can be ascribed to the quality of the dispersion and distribution of CNCs within the studied matrices. Some of the useful rheological measurements that are sensitive to interactions between the nanoparticles are presented in the next sections.

### 13.4.2 Small-amplitude Oscillatory Shear (SAOS)

Transition from a liquid-like behavior for neat polymer matrices to a solid-like behavior for nanocomposites and large increases of the dynamic rheological properties, such as complex viscosity, storage and loss moduli for nanocomposites relative to those of matrices, especially at low frequencies, are among the main effects caused by CNCs when they are nano-dispersed and well-distributed. Figure 13.4 clearly demonstrates these changes for solvent-cast PLA–CNC nanocomposites with different CNC loadings relative to the neat polymer matrix. The complex viscosity of the neat polymer matrix exhibits a long plateau, with a slight shear-thinning behavior at high frequencies (Figure 13.4a) and its storage modulus is typical of molten polymers with a terminal zone of slope equal to 2 on the log–log plot (Figure 13.4b). However, by incorporating CNCs, significant increases in the complex viscosity and storage modulus are observed, mainly at low frequencies, demonstrating clearly the strong effect of CNCs on the rheological properties of the polymer matrix. It is also worth mentioning that as the CNC concentration increases in the system, the possibility of agglomerate formation significantly increases and lower rheological properties may be expected as illustrated in Figure 13.4a and b for PLA containing 7 wt% CNCs compared to PLA with 6 wt% CNCs. The behavior of polymer nanocomposites in the low-frequency region is governed by the interactions between the nanoparticles and the formation of an interconnected network of nanoparticles [20]. At the percolation threshold, the nanocomposites exhibit a transition from liquid- to solid-like behavior with a complex viscosity tending to infinity as the frequency goes to zero and plateau values for the elastic modulus. An estimation of the rheological percolation threshold can be obtained from SAOS data by plotting the complex viscosity as a function of the complex modulus as shown in Figure 13.4c for PLA and PLA–CNC. For the neat polymer matrix and composites with CNC contents below the rheological percolation threshold, no viscosity upturn is observed at low frequencies, while at larger CNC loadings, the unbounded viscosity is indicative of a percolating network and an apparent yield stress [18, 20, 49–52]. Therefore, the rheological percolation threshold would fall in the range of CNC loadings with no complex viscosity upturn and the first point for which upturn is observed. Moreover, the modified Herschel–Bulkley model can fit the SAOS data for samples with CNC contents above the percolation threshold concentration well:

$$\eta^* \equiv \frac{G^*}{\omega} = \frac{\sigma_0}{\gamma^0 \omega} + k(\gamma^0 \omega)^{n-1} \quad (13.2)$$

where  $G^*$  is the complex modulus,  $\sigma_0$  is the apparent yield stress,  $\gamma^0$  is the strain amplitude,  $k$  is a constant, and  $n$  is the flow index [18]. Thus, the apparent yield stress can be determined from the modified Herschel–Bulkley model and used as a



measure of the CNC network strength. The higher the value of the apparent yield stress, the stronger the network. The rheological percolation threshold can be determined using storage modulus data at low frequencies as reported in Figure 13.4d for solvent-cast PLA-CNC nanocomposites with different CNC loadings [20]. Then, the following empirical power-law equation can be used to fit the data and obtain the rheological percolation threshold [53]:

$$G' = \beta_{cG} \left( \frac{m - m_{cG}}{m_{cG}} \right)^n \text{ for } m > m_{cG} \quad (13.3)$$

where  $\beta_{cG}$  and  $n$  are power-law constants,  $m$  is the CNC concentration (wt%), and  $m_{cG}$  is the rheological percolation threshold (wt%) [20, 53]. A value of 0.68 wt% was reported for the rheological percolation threshold of solvent-cast PLA-CNC nanocomposites [20].

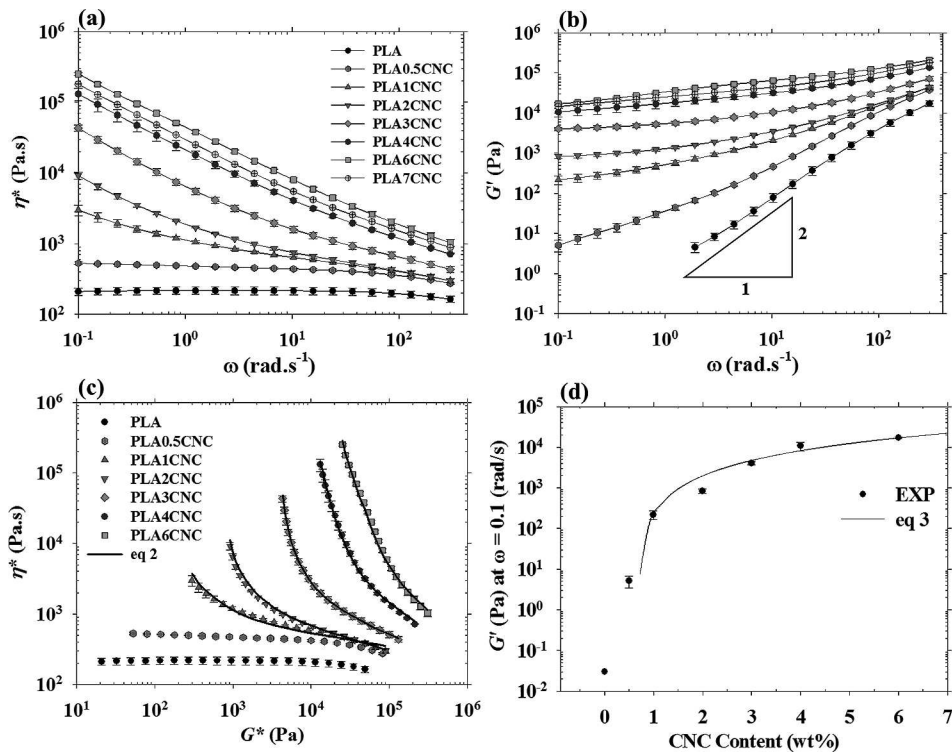


**Figure 13.4** SAOS data for PLA and PLA-CNC nanocomposites prepared via a solvent-casting method for various CNC loadings. (a) Complex viscosity,  $\eta^*$ , and (b) storage modulus,  $G'$ , versus frequency,  $\omega$ , (c)  $\eta^*$  versus complex modulus,  $G^*$ , and (d)  $G'$  as a function of CNC loading. The lines in c and d are the fits of the modified Herschel-Bulkley model, Equation (13.2) and Equation (13.3), respectively (adapted from [20])

### 13.4.3 Steady Shear

Similar to the behavior shown in SAOS experiments, shear thinning without any plateau region and unbounded viscosity at low shear rates for polymer–CNC nanocomposites are expected in steady-shear tests, while the neat polymer matrices usually exhibit a plateau region at low shear rates. Figure 13.5a illustrates the effect of CNC content on the viscosity of PLA and PLA–CNC nanocomposites with different CNC loadings. A long plateau region for the matrix is observed, as expected, while by the addition of CNCs, the plateau region disappears and a shear-thinning behavior is observed. At higher CNC contents, as the distance between the particles decreases, the interactions between CNCs become stronger and the possibility of network formation increases; as a result, increased viscosity values with a more pronounced shear-thinning behavior are observed for larger CNC loadings. For these samples, the shear viscosity significantly decreases with increasing shear rate (Figure 13.5a) indicating that the CNC network is broken down under shear [20]. Figure 13.5b compares the PLA–CNC systems with the same CNC concentrations, but for different preparation methods. A better dispersion and distribution contribute to a stronger CNC network and higher viscosity values are observed when the nanocomposite is prepared with a masterbatch method and melt-extruded utilizing a twin-screw extruder. However, the neat PLA and PLA–CNC composites prepared without a solvent-cast masterbatch, i.e., DMI and DME, exhibit very low viscosity values and almost a Newtonian behavior confirming that the direct melt-mixing method is not efficient in dispersing CNCs into the PLA matrix.

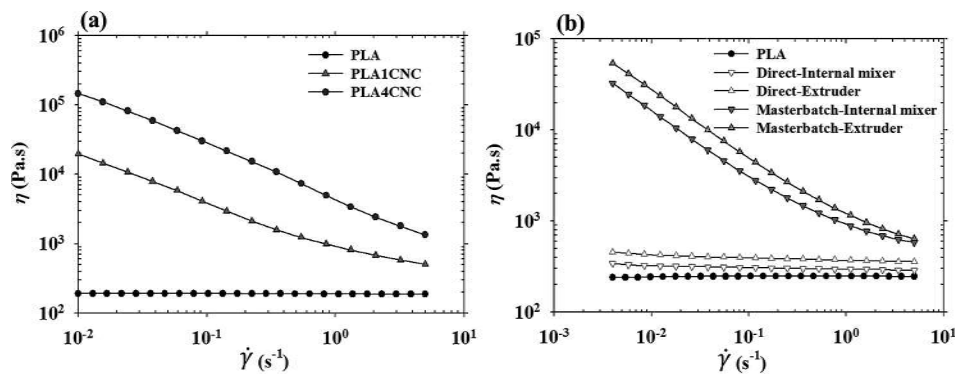


**Figure 13.5** Steady-shear viscosity,  $\eta$ , versus shear rate,  $\dot{\gamma}$ , for: (a) PLA, and PLA with 1 and 4 wt% CNCs prepared via a solvent-casting method [20], and (b) PLA, PLA–CNC composites prepared via direct melt mixing utilizing an internal mixer or a twin-screw extruder, and PLA–CNC nanocomposites prepared using solvent-cast PLA–CNC masterbatches that were melt-mixed with PLA employing an internal mixer or a twin-screw extruder [18]

### 13.4.4 Transient Behavior

Another rheological measurement that can be utilized to obtain information about the quality of the CNC dispersion, efficiency of the preparation method, and consequently, the existence and strength of the CNC network is the transient (also called start-up or stress growth) shear test. In this experiment, a sudden and constant shear rate is applied and the variation of the transient viscosity,  $\eta^+$ , of the samples with time is monitored. Figure 13.6a depicts how CNCs can change the behavior of a PLA matrix in such measurements by comparing the variation of  $\eta^+$  with time for PLA and PLA-CNC composites prepared with direct melt mixing and combined solvent-casting and melt mixing [18]. The neat matrix and the composites without a CNC network, i.e., those prepared with direct melt mixing, do not show any overshoot due to the absence of any structure and their low viscoelasticity. For polymer-CNC nanocomposites prepared using a solvent-cast PLA-CNC masterbatch, however, overshoots are observed at the beginning of the tests and are attributed to the structure or network of CNCs within the polymer matrix [18, 20, 21]. These transient tests are destructive, and when the structure is broken down, the samples exhibit a steady-state viscosity. However, Figure 13.6b shows that when a reverse shear flow is suddenly imposed, the structure can be rebuilt depending on the rest

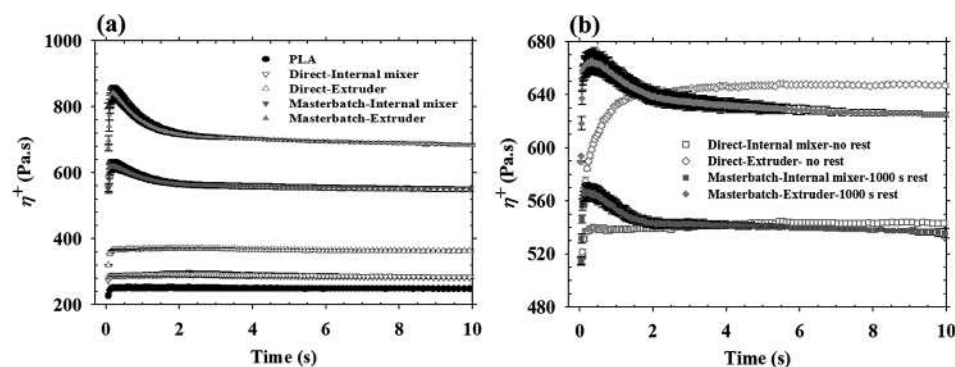


**Figure 13.6** (a) Transient viscosity in shear stress growth as a function of time performed under a shear rate of  $5 \text{ s}^{-1}$  for PLA, PLA-CNC composites containing 4 wt% CNCs and prepared with direct melt mixing, batch and extrusion, and melt mixing of solvent-cast PLA-CNC masterbatch with PLA, and (b) transient viscosity for the same samples in reverse flow tests right after the cessation of the first shear test, and after 1000 s rest time (adapted from [18])

time. If the rest time is sufficiently long, for example 1000 s as shown in Figure 13.6b, particle-particle interactions increase and, consequently, the structure is gradually rebuilt and eventually, the initial structure as before the shear test is recovered [18, 20]. Again, for the PLA-CNC composites prepared with direct melt mixing, there was no evidence of CNC network formation after the rest time and